Applied Catalysis B: Environmental 298 (2021) 120527

Contents lists available at ScienceDirect

Applied Catalysis B: Environmental

journal homepage: www.elsevier.com/locate/apcatb

Influence of alkali metal cations on the photoactivity of crystalline and exfoliated amorphous WO_3 – photointercalation phenomenon

M. Szkoda [a,b,*], K. Trzciński [a], G. Trykowski [c], M. Łapiński [b,d], A. Lisowska-Oleksiak [a]

[a] Faculty of Chemistry, Department of Chemistry and Technology of Functional Materials, Gdańsk University of Technology, Narutowicza 11/12, 80-233, Gdańsk, Poland
[b] Advanced Materials Center, Gdańsk University of Technology, ul. Narutowicza 11/12, 80-233, Gdańsk, Poland
[c] Faculty of Chemistry, Nicolaus Copernicus University in Toruń, Gagarina 7, 87-100, Toruń, Poland
[d] Faculty of Applied Physics and Mathematics, Gdańsk University of Technology, Narutowicza 11/12, 80-233, Gdańsk, Poland

ARTICLE INFO

Keywords:
WO_3
Exfoliation process
Photointercalation
Photoelectrocatalysis
Water splitting

ABSTRACT

In order to investigate the effect of photointercalation on photoelectrochemical properties, two types of WO_3-based photoanodes, bulk and exfoliated have been prepared and investigated. An aqueous exfoliation method is introduced for the simple fabrication of amorphous and hydrated WO_3 nanomaterial using commercial bulk WO_3 precursor. The comparison of obtained material with bulk WO_3 was performed using Raman, UV–vis, and XPS as well as scanning and transmission electron microscopies. The photoelectrochemical and photocatalytic performances of bulk and exfoliated WO_3 were compared. Generally, the proposed exfoliation procedure led to the preparation of photo(electro)catalyst characterized by better performance measured as a photocurrent of water oxidation and rate of methylene blue photodecomposition. The main aim of this research was to investigate the influence of alkali metal cations (Li^+,Na^+,K^+,Cs^+) presence in electrolyte on the photocatalytic and photo (electro)catalytic activity of the samples in a form of suspended powder and thin layer on transparent-conductive substrate (FTO), respectively.

1. Introduction

The concept of photointercalation, first proposed and explored by Tributsch in 1980, relates to a photoactive semiconductor having a layer structure, which can store light excited charges accompanied by ion intercalation under the illumination [1]. This phenomenon can be used in photo-intercalation solar cells that would store the stored energy and release it during the night. Mostly, the studies concerned semiconductors showing p-type conductivity and were based on photocathodic intercalation of cations [2]. Interestingly, the effect of photoinduced cation intercalation may occur also under anodic conditions as it was shown for n-type MoO_3 grown on molybdenum substrates [3]. There is also a possibility of the layered metal oxide utilization as an energy storage material in photobatteries as it was shown for the case of CdS-decorated WO_3 film photocharged in lithium-ion containing electrolyte [4]. Thus, it may suggest that the effect of photointercalation of cations from the electrolyte should be taken into account for other n-type photoanodes exhibiting layered structure. One of them is tungsten oxide, which is commonly tested as a photoanode for water photooxidation [5–8]. Tungsten trioxide is known also as a photochromic and electrochromic compound. Its wide energy gap allows to absorb light from the UV range. The photochromic effect in tungsten oxide is closely coupled to photo excited electron (e-) hole (h+) pairs which can decompose water molecules being incorporated in WO_3 to a substantial amount. The light-induced oxidation of H_2O molecule can be written as: $H_2O + 2h^+ \rightarrow O + 2H^+$ which describes the creation of protons (H^+) and metastable oxygen radicals O [9]. The protons and optically generated electrons allows the formation of coloured tungsten bronze which relay on an intercalation of proton into oxide structure and valence changes of metal ion: $WO_3 + xH^+ + xe^- (CB) \rightarrow H_xW_x^{+5}W_{1-x}^{6+}O_3$. Photointercalation of other univalent and some divalent cations is expected to occur under illumination, depending on their presence in the semiconductors' vicinity. The intercalation can be driven also electrochemically as is presented in fundamental works on the role of electrochemically driven intercalation process's on lithium ions batteries functioning, by Goodenough and Whittingham, Nobel prize winners

* Corresponding author at: Faculty of Chemistry, Department of Chemistry and Technology of Functional Materials, Gdańsk University of Technology, Narutowicza 11/12, 80-233, Gdańsk, Poland.
E-mail address: mariusz.szkoda1@pg.edu.pl (M. Szkoda).

https://doi.org/10.1016/j.apcatb.2021.120527
Received 17 May 2021; Received in revised form 6 July 2021; Accepted 11 July 2021
Available online 13 July 2021

[10–12].

Electrochemically driven intercalation, causing colour changes of the WO_3 host, is discussed in ref. [13]. This review paper by Granquist presents the state-of-the-art in the field of electrochromic tungsten oxides films – review concerns period 1993−1998. Electrochemical intercalation/deintercalation process is controlled by slow diffusion of intercalated counter–ion in the solid-state and potential range of the film electrode [13].

The most popular scheme illustrating electrochromism is based on the cathodic process: $WO_3 + xM^+ + xe^-(CB) = M_xW_x^{+5}W_{1-x}^{6+}O_3$. (M – metal cations), where electrons are taking part in valence changes of transition metal ions forming layered (or spinel) oxides. Granquist pointed out that presented equation neglects many facts, for example, hydration of the film and surface states of the examined semiconductor. Thus, the scheme should be treated as a robust simplification of the electrochromic reaction. As was proven for amorphous WO_3, ion trapping can limit reversibility of the intercalation process, which is found to be irreversible when x in Li_xWO_3 is above~ 0.65 value [14].

Moreover, photointercalation, as also electrochemically driven intercalation, is affected by the orientation of the crystal as it was shown for MoO_3 [3] and for WO_3 [15]. The same group gave evidence for the immense influence of crystal disorder on the process. As reported in Ref [3]. crystallographic structure and band structure of MoO_3, as should be also for WO_3, enables to generate excited charges for reductive reaction upon photo-excitation and store part of the excited charges in a host crystal via bronze formation. The stored charge is shown to be released for utilization in the dark in a kind of photoelectrochemical cell (PEC) [4]. The photocatalytic activity of MoO_3 is strongly affected by photointercalation The effect of K^+ photointercalation into MoO_3 thin films and its effect on optical properties, morphology as well as photoactivity have been reported [16,17]. The process of Mo-bronzes formation was carried out under simulated solar light illumination during the anodic polarization (+0.5 V vs. Ag/AgCl) of the electrode, at the potential that deintercalation is expected [17]. The effect of photointercalation of cations from the electrolyte should be taken into account for other photoanodes exhibiting layered structure as well. The intercalation into the van der Waals gaps is one of the methods of layered materials modification. Usually, the WO_3 layers were modified before the actual photoelectrochemical experiment, *e.g.* cathodic polarization of WO_3-based electrode performed in acid electrolyte led to the formation of protonated WO_3 films. The modification hindered the photoactivity measured as the photocurrent of water oxidation, however, under the conditions of water splitting measurement, deintercalation occurred and the electrode returned to its initial state [18]. There was also a successful attempt of Li^+, Na^+, and K^+ electrochemical intercalation, which in all cases results in an enhanced photocurrent density in comparison with the unmodified WO_3 photoanode. However, the stability of intercalated photoelectrodes was not investigated [19]. The theoretical studies on the alkali metal cations (Li^+, Na^+, K^+, Cs^+ Rb^+) intercalation into WO_3 structure and data on changes in electronic properties were reported. Valentin and co-workers calculated insertion of alkali metal cations as interstitial dopants in WO_3 structure, showing immense distortion in the structure and significant reduction of the bandgap energy [20]. Moreover, recently computational studies on H^+, Li^+, Na^+ cations intercalation into WO_3 were presented [21]. Authors discussed changes in electronic structure, the optical properties and diffusion behaviors of colored state of WO_3 materials using first principle calculations.

Solarska and co-workers reported influence on cation doping (using lithium, silicon, ruthenium, molybdenum and tin) into WO_3 on morphology and photoelectrochemical activity of WO_3-doped photoanode [22]. Moreover, it has been demonstrated that the intercalation of N_2 – a neutral molecule to the WO_3 structure positively affects the photoactivity of thermally stable photoanodes [23,24]. Reduced energy bandgap, increased charge carrier density and improved photocurrent of water photooxidation have been achieved for barium ions intercalated into WO_3 photoanodes, prepared via hydrothermal method [25]. Systematic studies on the photoactivity of hydrothermally prepared WO_3 nanostructures like nanoplates, nanorods, nanoneedles and nanowires proved that morphology has a great impact on photoactivity. The bandgap energies of synthesised WO_3 nanostructures were ranged from 2.70 +−0.03 eV to 3.25 ± 0.03 eV [26]. It has been shown that the photocatalytic activity of nanocrystalline WO_3 is a compromise of the bandgap, crystal phase, morphology, and the oxidation state of tungsten [26].

It can be concluded on the basis of previous reports that intercalation phenomenon can strongly affect pretreated photoanode materials working under anodic conditions e.g. during photoelectrochemical water splitting. On the other hand, it was shown that intercalation can be caused by illumination, even at the potential range that deintercalation is anticipated [17]. Thus, in this work we are focused on the influence of photointercalation of chosen alkali metal cations during photoelectrochemical water oxidation into WO_3 photoanodes. In order to investigate this effect, the photoelectrochemical and photocatalytical results were performed for two types of electrode films, bulk monoclinic WO_3 as well as amorphous WO_3 obtained via long term aqueous suspension heating process, supposed to lead to exfoliation of bulk WO_3.

2. Experimental

2.1. Chemicals

All the reactants and solvents were of analytical grade and used without further purification. The WO_3 powder, polyethylene oxide (M = 300 000), tert-butyl alcohol, benzoquinone, silver nitrate, ammonium oxalate, Li_2SO_4, Na_2SO_4, K_2SO_4 and Cs_2SO_4 as well as fluorine-doped tin oxide (FTO, 7 Ω/sq) were purchased from Sigma.

2.2. Characterization techniques

2.2.1. Morphology and crystal structure

The crystal structure of the obtained materials was examined by powder X-ray diffraction (XRD). Patterns were obtained using an X`Pert Pro diffractometer with X`Celerator detector and Cu Kα radiation, λ =0.15406 nm. Raman spectroscopy measurements were performed using 514 nm laser using 1% of its total power (InVia, Renishaw). Ten spectra in the 100-1200 cm^{-1} range were collected and averaged for each sample using 100x objective. The surface morphology was studied using SEM using Quanta 3D FEG (Fei Company) and TEM using Tecnai 20 F X-Twin (Fei Company). The chemical composition of the surface of bulk and exfoliated samples was performed using an Argus Omicron NanoTechnology X-ray photoelectron spectrometer. The UV–vis spectra of bulk and AH-WO_{3-x} were recorded using a Perkin Elmer Lambda 18 UV–vis spectrometer. The optical band gap of the obtained material was determined as the intercept of the tangent of the plot of transformation of the Kubelka–Munk function ($KM^{0.5}E_f^{0.5}$) vs. photon energy, where KM = $(1R)^2/2R$, R – reflectance.

2.2.2. Photoelectrochemical and photocatalytic measurements

The photoelectrochemical measurements were performed in an electrochemical cell equipped with a quartz window. The geometrical surface area of the electrodes was equal to ~ 0.7 cm^2. A high-pressure 150 W xenon lamp (LOT – QuantumDesign GmbH) with the AM1.5 G filter was used as a source of electromagnetic radiation. The light intensity was adjusted to 100 mW cm^{-2} and was controlled by an Ophir power meter. The measurements were performed in different aqueous electrolytes (0.1 M Li_2SO_4, Na_2SO_4, K_2SO_4 and Cs_2SO_4). Platinum mesh and Ag/AgCl (3 M KCl) act as counterelectrode and reference electrode, respectively. The electrochemical studies were conducted using the AutoLab PGStat204 potentiostat-galvanostat system (Methrom, AutoLab). The Mott-Schottky analysis was performed on the basis of impedance spectra recorded using Ivium Vertex potentiostat/galvanostat. The space charge capacitances were estimated on the basis on the

single frequency impedance (1000 Hz). The photocatalytic activity of the samples (50 mg of powder) was investigated throughout the degradation progress of methylene blue (MB). The volume of MB aqueous solution used in the experiment was 50 mL with an initial concentration of 10^{-5} M. The changes of MB concentration during measurement were determined according the absorbance measurement at $\lambda = 665$ nm wavelength using the UV–vis spectrophotometer model UV5100 (Metash). In order to test the mechanism of photocatalytical degradation of methylene blue on bulk and exfoliated WO_3, process was performed in the presence of different alkali metal cations (Li^+, Na^+, K^+, Cs^+) as well as in the presence of appropriate scavengers. Tert-butyl alcohol (t-BuOH), $AgNO_3$, ammonium oxalate (AO), and benzoquinone (BQ), acted as scavengers of hydroxyl radicals, electrons. holes and superoxides, respectively.

3. Results and discussion

3.1. Synthesis and electrode preparation

The procedure that leads to the formation of an amorphous and hydrated WO_3 was described in our previous reports [27,28]. Generally, the aqueous suspension of bulk WO_3 was subjected to an exfoliation procedure for 10 days at 80 °C. In order to perform the synthesis, 3 g of WO_3 was suspended in 50 mL of triple-distilled water. WO_3 after exfoliated procedure is named as AH-WO_3. The UV–vis spectrum of exfoliated WO_3 aqueous suspension is characterized by strong absorbance appearing from 350 nm and extending to lower wavelengths (Fig. S1). The lack of the absorption edge characteristic for the energy band gap of crystalline, bulk WO_3 (absorption edge at about 500 nm) suggests that the exfoliation procedure leads to the preparation of amorphous WO_3. In order to obtain AH-WO_{3-x} in a form of a powder, water from exfoliated mixture was slowly evaporated from the Petri dish at 40 °C for 24 h. Next, the obtained powder was subjected to DSC (differential scanning calorimetry) measurements, see Fig. S2. Such material was tested as photocatalyst for methylene blue degradation. Similarly, to prepare the film of AH-WO_{3-x} on the transparent-conductive substrate, the 50 µl (on the area of 1cm^2) of exfoliated WO_3 suspension was drop-casted on the degreased FTO substrate and heated at 40 °C.

In order to test bulk WO_3 as a photocatalyst, commercially available WO_3 powder was grinded in a mortar and pestle. The bulk WO_3 thin films were prepared on FTO substrates using dip-coasting method with PEO as a binder. The material-to-binder mass ratio was equal to ~2. Then, water was added to the mixture (1 mL for 0.2 g of the material) and homogenized using a glass rod. The FTO substrate was immersed in the suspension for 3 s and slowly pulled out. The non-conductive side was cleaned with dust-free tissue (Kimtech). Then, the resulting film was dried at room temperature for 2 h and annealed in an air atmosphere at 400 °C to remove the binder. The procedure of solid material thin layers deposition on the substrate was described in more details in the previous paper [29]. In both cases, the uncovered part of FTO was attached with the copper electrical tape (3 M) and isolated using parafilm.

3.2. Morphology

In order to investigate the changes of WO_3 morphology caused by exfoliation procedure, SEM and TEM were used. The morphology change from micrograins (bulk WO_3) to nanoplates (AH-WO_3) is clea0rly demonstrated in SEM micrographs presented in Fig. 1a-e. Bulk WO_3 occurs in a form of irregular crystallites (Fig. 1a). Higher magnification images reveal its layered structure, as expected (Fig. 1b).The exfoliation procedure significantly affects the material morphology. The AH- WO_3 appears in a form of rounded-shape clusters (Fig. 1d). They are built by agglomerated nanoplates that were probably formed during slow water evaporation. As presented in Fig. 1e, many nanoplates with morphology similar to scraps of paper can be observed, which is in obvious contrast to that of bulk WO_3 (irregular crystallites, Fig. 1a). The thickness of the nanoplates can be estimated to be from 50 to 150 nm. The detailed morphology investigation of the WO_3 materials were performed using transmission electron microscopy, see Fig. 1c and f. Micrographs presented in Fig. 1c (and Fig. 2c inset) exhibit the typical TEM images of nanoparticles (bulk WO_3). The comparison of SEM and TEM images show large size distribution of bulk WO_3. In the case of exfoliated

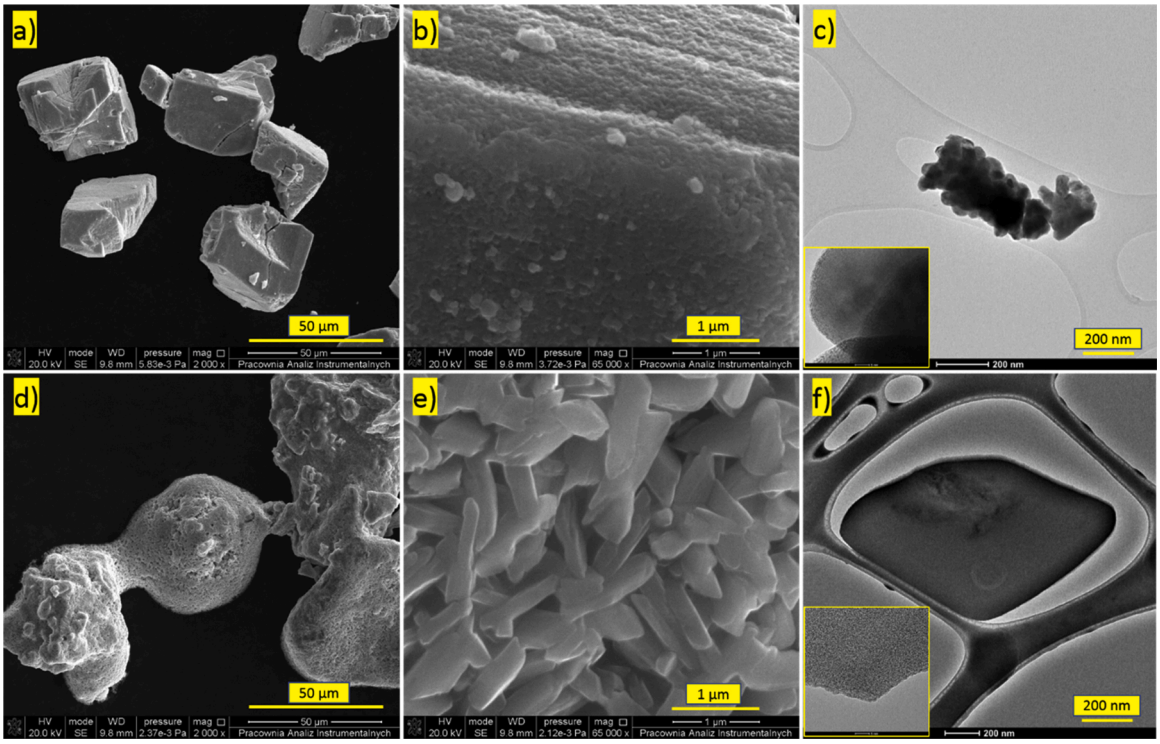

Fig. 1. SEM images of (a, b) bulk WO_3 and (d, e) amorphous and hydrated WO_3. TEM images of c) bulk WO_3 and e) exfoliated material.

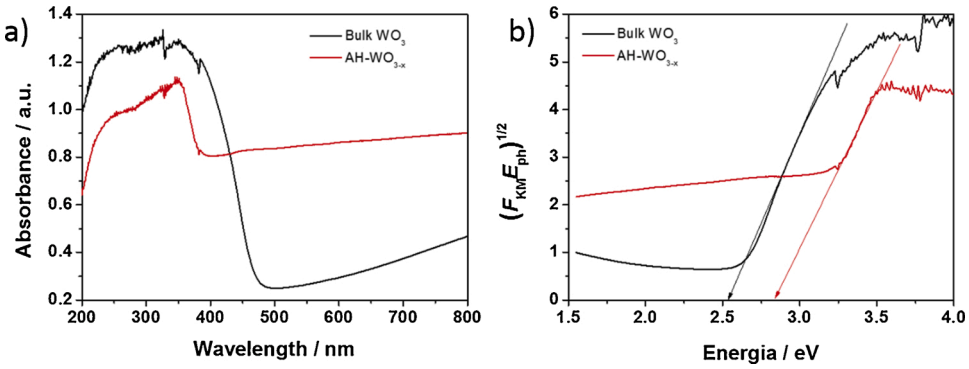

Fig. 2. a) The UV–vis absorption spectra and b) the Tauc plot for bulk and hydrated WO_3 films.

material, TEM images demonstrated the presence of many ultra-thin layers with several-hundred nanometers of length. Such semi-transparent layers are shown in Fig. 1f (and Fig. 1f inset).

The EDX analysis for bulk and exfoliated material (Fig. S3) confirms the presence of tungsten and oxygen (the signal of Cu origins from copper mesh that was used as a support for TEM measurement). The elemental composition shows that the W:O ratio in exfoliated WO_3 (Fig. S3a) differs from the ratio of these elements in bulk material (Fig. S3b) due to the modification procedure. The higher W:O atomic ratio after exfoliation procedure suggests material reduction and formation of nonstoichiometric suboxide WO_{3-x}. The presence of hydrogen in the samples was estimated by means of elemental analysis. The material after exfoliation procedure contained 2.478 at% hydrogen, and bulk WO_3- 0.235 at%.

3.3. Spectroscopic methods

In Fig. 2a and b the absorbance spectra and Tauc plots are given, respectively. As it is typical for tungsten oxide, the highest absorbance was registered in the UV range. In the case of the exfoliated material (solution slowly dried in a Petri dish), the absorbance edge is shifted towards lower wavelengths. Simultaneously the UV–vis spectrum of this sample is characterized by higher absorption at Vis range of electromagnetic irradiation, which is positive for the photocatalytic materials in processes involving sunlight (the photocatalytical and photoelectrochemical applications). Similar behavior at visible range was already reported for other metal oxides e.g. hydrogenated TiO_2 and thermally treated Mo/MoO_3 samples. It can be attributed to the formation of the suboxides, which are characterized by the presence of reduced metal centres like Ti^{3+} and Mo^{5+} respectively [30,31].

The absorption band of WO_{3-x} in the visible and near-infrared region of the spectrum is commonly described as a surface plasmon resonance (SPR) effect. A clear band with a maximum in a visible region was reported for reduced WO_3 in a crystalline form [32–35]. On the other hand, broad absorption at wavelengths higher than the energy bandgap, as in the presented case, was shown for amorphous WO_3 samples [36,37]. Thus, the SPR absorption in the case of exfoliated WO_3 cannot be excluded. However, since the plasmonic absorption strongly depends on the shape and the size of the nanomaterials [38,39], the lack of sharp peak can be also related to the wide size distribution of the obtained flakes. Nevertheless, the origin of the absorption in a visible range of exfoliated WO_3 is not clear and it requires further investigations.

Basing on the Tauc plots (Fig. 2b), the optical bandgap (E_g) values were determined and equaled 2.54 and 2.84 eV for bulk and amorphous and hydrated WO_3, respectively. It was assumed that both samples exhibit indirect band gap as it was shown for bulk WO_3 [40]. The differences of E_g may be related to the crystallinity and lack of it of characterized materials as it was shown previously for sputtered WO_3 layers [41]. Thus, the exfoliated material has a higher optical band gap in comparison to the bulk material, however, one may expect that enhanced visible light absorption of exfoliated WO_3 will positively affect the photocatalytic properties.

The X-ray photoelectron spectroscopy allows investigating binding energies and changes in the oxidation states in the material due to the modification process with reference to the bulk WO_3. The XPS spectra of the W 4f region are presented in Fig. 3. In the case of the bulk WO_3, the doublet at 37.97 and 35.83 eV was recorded and ascribed to the binding energies of the W $4f_{5/2}$ and W $4f_{7/2}$ orbital electrons of W^{6+}, respectively (Fig. 3a). After the formation of amorphous and hydrated nanoplates, two new peaks in the W 4f region appeared at the lower binding energies of 37.11 and 34.96 eV, belonging to the W^{5+} oxidation state [42]. The appearance of the W^{5+} valence state probably associated with the presence of oxygen vacancies in the exfoliated material and therefore, the chemical structure can be referred to as WO_{3-x} suboxide. It is very likely that during the formation of the oxygen-deficient structure, the W^{6+}center neighboring the oxygen vacancy in the WO_3 lattice is reduced to W^{5+}. A similar phenomenon of metallic center reduction was observed for exfoliated molybdenum trioxide [43].

The O1 s peak was deconvoluted in two components in the case bulk WO_3 (O1 sA and O1 sb) and three components in the case exfoliated WO_3 (O1 sA, O1 sB and O1 sC), see Fig. 3b. The peak O1 sA with a binding energy of 530.4 eV is the same for both spectra and is assigned to the oxygen atoms (O^{2-}) that form the strong W═O bonds [44]. The peak at 531.6 eV (O1 sB) corresponds to OH-groups [45], however it may illustrate the C contamination and can be more precisely attributed to C═O bonds [46]. The signal is shifted into the higher binding energy for AH-WO_{3-x} nanoplates suggesting different chemical surrounding. The intensity is higher in comparison to spectrum of bulk WO_3 due to the higher concentration of surface groups. The peak at the highest binding energy (O1 sC, 533.4 eV) observed only in the case of exfoliated material is attributed to water molecule bound at the surface of the samples, proving the existence at the surface of $WO_3(H_2O)_n$ phases [47]. The XPS results proving H_2O presence are consisted with Raman spectroscopy.

3.4. Material structure

The crystal structure of the samples was examined locally on TEM images. Fast Fourier transform (FFT) was made from the marked areas in Fig. 4a, b. In the presented FFT images, a clear crystal structure for the starting material was observed (Fig. 4b), periodic point reflections) or an amorphous structure (Fig. 4d, no point reflections) for exfoliated WO_3 was observed.

Raman spectroscopy was used for characterization of the bulk and exfoliated WO_3 samples. As can be seen in Fig. 5, the two normalized spectra are very different from each other. In the case of bulk WO_3, all the peaks are sharp and well defined due to the crystalline nature (monoclinic phase) of the metal oxide. It can be seen from Fig. 5 (black line), that the most intense peaks are observed at 807 and 716 cm^{-1}, and they can be related to the symmetric and asymmetric vibrations of W^{6+}–O bonds (O—W—O stretching modes), while the band at 273 cm^{-1}

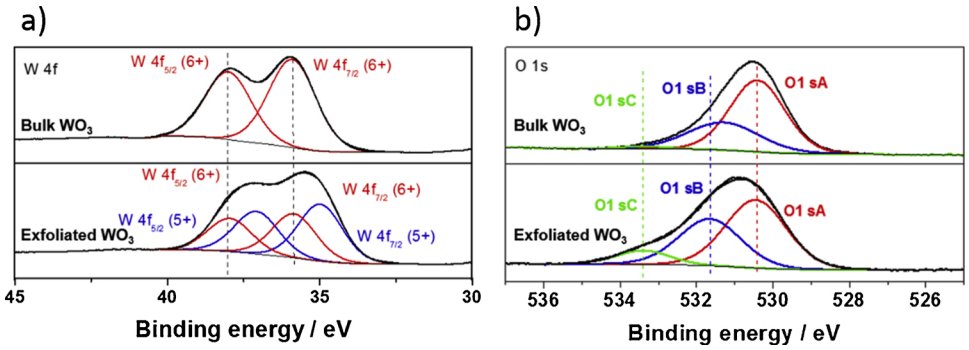

Fig. 3. Deconvoluted XPS spectra of the bulk and hydrated material: a) W 4f and b) O 1s regions.

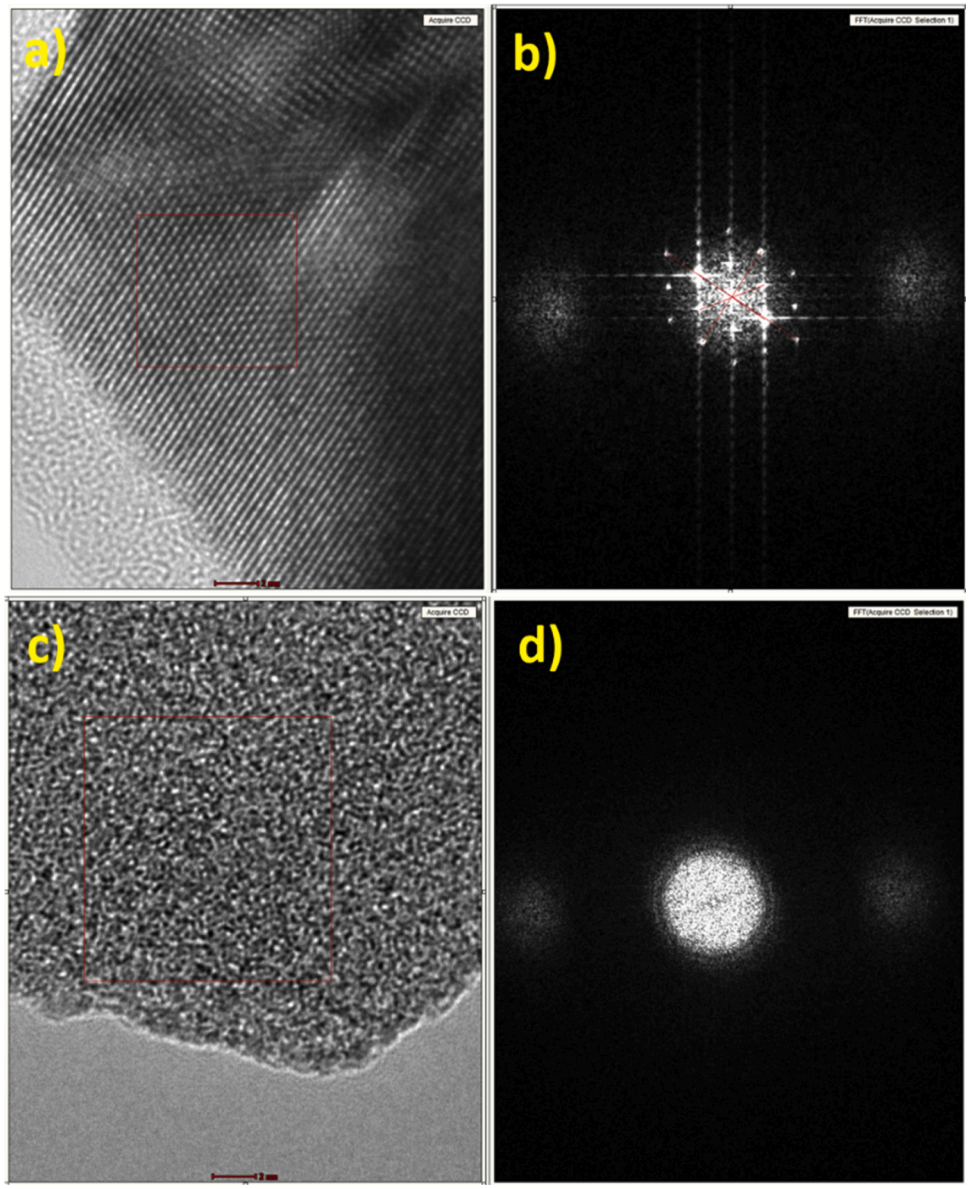

Fig. 4. TEM images and FFT of bulk WO_3 (a, b) and AH-WO_3 (c, d).

can be ascribed to the δ (W—O—W) bending mode of the bridging oxygen of monoclinic phase [48]. In the case of the spectrum of AH-WO_3, the registered band confirms the presence of hydrated $WO_3 \cdot H_2O$ [49]. The intensity of the bands are much weaker and broader in comparison of the spectrum of crystalline WO_3 due to the disorder nature of hydrated material. The main band is located at 961 cm^{-1} and can be attributed to the W—OH vibrations on the surface of nanoplates. Similar band was observed in the Raman spectra of WO_3 hydrates [50]. Water

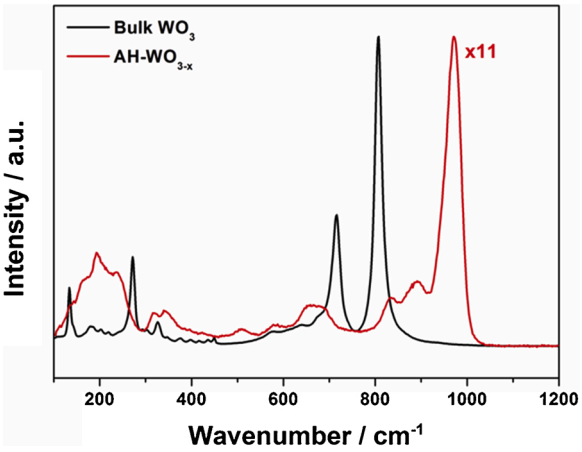

Fig. 5. Raman spectroscopy of bulk and exfoliated material.

molecule binds with oxygen of WO_6 octahedra giving a contraction of the opposite W—O bond [51,52]. Cazzanelli et al. observed a similar Raman band after long milling of micro-crystallized tungsten oxide powder leading to the significant particle size decrease. This band was attributed to the occurrence of $W^{5+}O_2$ surface bonds [53]. Thus, high surface to volume ratio of WO_3 nanoplates and lack of crystallinity make Raman spectrum affected mainly by short-range ordering of W—OH vibrations on the nanostructures edges as opposed to bulk WO_3. The wide, low-intensity band at 660 cm^{-1} may indicate the WO_3 nanoplates thickness and hydration level, as it was previously reported by Kalantar-Zadeh et al. [49], since it can be attributed to the stretching modes of O—W—O for the bridging oxygen atoms across WO_3 planes. The low intensity of this band confirms the successful exfoliation of WO_3 structure.

The phase composition and crystal structure of bulk and modified samples were also examined by powder XRD technique (see Fig. S4). In the case of bulk WO_3, the peaks at 2θ values at 23.07, 23.7, 24.4, 26.6, 28.8, 33.3, 34.2, 35.6, 41.8, 47.3, 50, 54.2 and 56° corresponded to the (002), (020), (200), (120), (112), (022), (202), (103), (222), (040), (440), (240) and (241) crystal planes of monoclinic phase of WO_3 were found. The XRD pattern of bulk WO_3 consists all reflexes that are characteristic for monoclinic phase of tungsten trioxide [54,55]. The XRD pattern of WO_{3-x} consists mainly amorphous halo, thus the exfoliated material loses its crystallinity. However, low-intensity peaks can be found (marked with diamonds and hearts in the figure). These peaks can be assigned to both orthorhombic-tungsten trioxide hydrate ($o\text{-}WO_3{\cdot}H_2O$) and hexagonal tungsten oxide hydrate ($h\text{-}WO_3{\cdot}0.33H_2O$) [56].

3.5. Electrochemical, photoelectrochemical and photocatalytic properties

Cyclic voltammetry was used for the electrochemical characterization of the WO_3 films on the FTO substrates. The electrochemical tests were performed in a three-electrode cell with 0.1 M K_2SO_4 aqueous solution as the electrolyte. As shown in Fig. 6a and b, the cyclic voltammetry (CV) of exfoliated and bulk WO_3 are compared at a scan rate of 50 mVs^{-1}. The CV curve of bulk WO_3 exhibits oxidation/reduction peaks that was observed previously and described as conversion of valence states of W-centers with simultaneous adsorption/desorption of cations available in the electrolyte [57]. The presence of anodic peak is an evidence that during oxidation of W^{5+} centers, the deintercalation of cation occurs simultaneously [58,59]. Interestingly, in the case of exfoliated material the oxidation peak was not observed. Instead of that, current plateau characteristic for pseudocapacitance was recorded.

The photoactivity of obtained electrodes were compared during potentiodynamic polarization in 0.1 M K_2SO_4 under intermittent irradiation using solar simulator. The LSV curves are presented in Fig. 7a. WO_3 exhibits n-type semiconducting properties, thus can be used as a photoanode for water photooxidation [40]. In the case of bulk WO_3, photocurrent is definitely lower compared to the photocurrent generated by hydrated WO_3 in measured potential range At a potential of about 0.5 V, the saturated photocurrent for exfoliated material was almost three times higher in comparison to that generated at the bulk WO_3. Thus, in the studied case, we observed a significant increase of photocatalytic efficiency of hydrated WO_3 nanoplates film than measured for the bulk WO_3. A slightly lower increase was reported when comparing pristine WO_3 with dehydrated crystalline plates WO_3 planes [60]. Our results indicate that the crystalline phase is not crucial for the photocatalytic activity of WO_3 nanomaterial and content of water is found as not a hindering factor as well. Thus, according to our best knowledge, it is the first to report on hydrated, amorphous phase exhibiting high anodic photocurrent, enabling further application in water splitting systems.

The results of photocatalytic degradation of MB by the WO_3 and $AH\text{-}WO_{3-x}$ suspended in aqueous solution of dye are presented in Fig. 7b. For comparison, a blank experiment under simulated sunlight irradiation without photocatalyst was also performed. After a 2 h illumination in the presence of bulk WO_3, the degradation of methylene blue reached 55 %, whereas the degradation efficiency of 83 % was achieved for exfoliated material. The improvement of the material's photoactivity in general results from the fact, that nanostructures obtained in the modification process: *i*) can improve charge carriers transport paths, *ii*) reduce the recombination rate of charge carriers and *iii*) increase the contact area of the photocatalyst with pollution due to the 2D nanostructure, which will increase the efficiency of organic contamination degradation in the water phase and increase in generated photocurrents

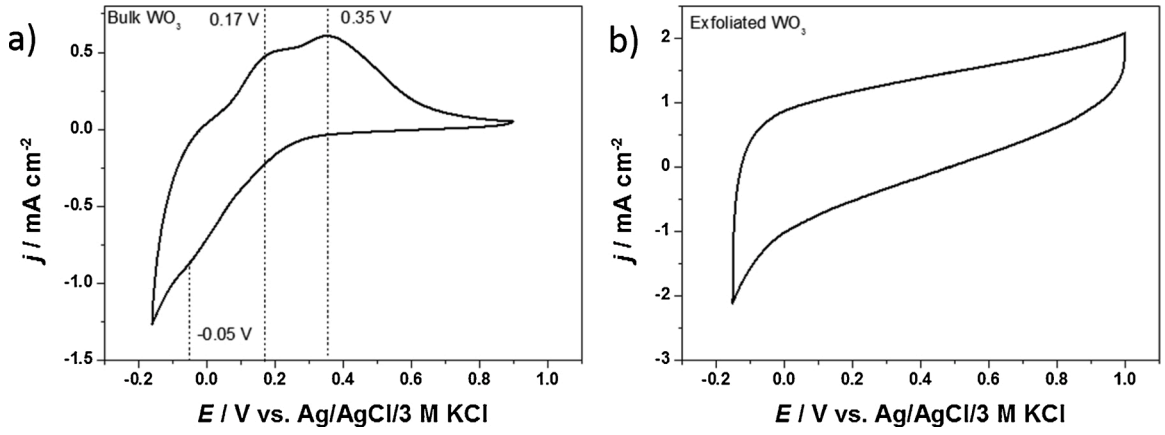

Fig. 6. Cyclic voltammograms for the a) bulk and b) exfoliated WO_3.

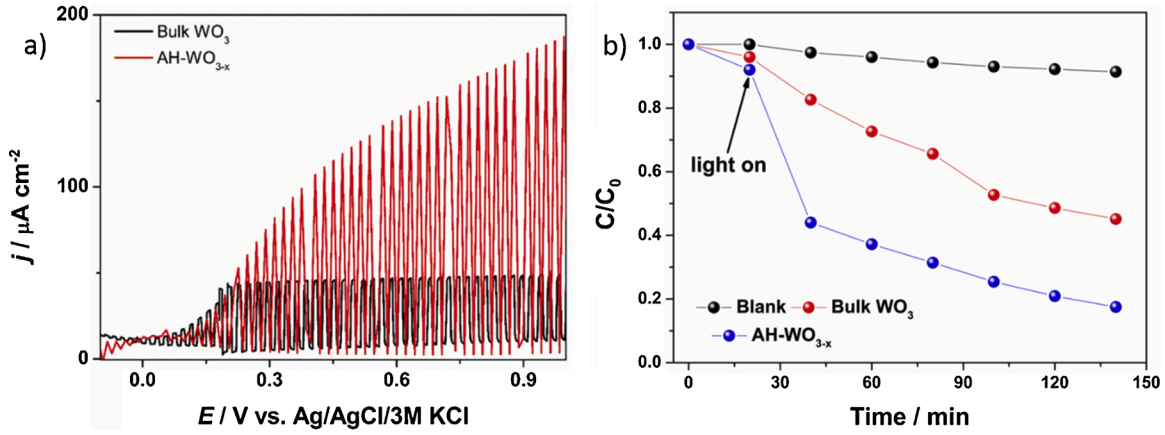

Fig. 7. a) The linear sweep voltammetry (LSV) (20 mV s^{-1}) recorded in 0.1 M K_2SO_4 under intermittent illumination for obtained electrodes. b) Photocatalytic performance of the catalysts under simulated sunlight irradiation (without addition of inorganic salt).

[61–63]. Notable, the amorphous and hydrated material also shows better adsorption properties, which is visible as a decrease in MB concentration after 20 min of stirring in the dark. It is related to the very high surface-to-volume ratio as well as surface enriched in surface groups. The wider optical energy bandgap may suggest worse photoactivity, however, it is not the case of bulk and exfoliated WO_3. As it was shown above (see Fig. 2), despite the E_g widening, the exfoliated material exhibits absorption ability in a whole visible range, which can positively affect photodegradation efficiency of organic pollutant. Thus, generally the proposed exfoliation procedure brings about novel material with enhanced photoactivity of tungsten trioxide.

3.6. The influence of photointercalaction on the photocatalytic and photoelectrochemical properties of bulk and exfoliated WO_3

Tungsten oxide is one of the most commonly investigated photochromic materials [64,65]. Since the photochromic effect of WO_3 is strictly related to the photo-induced cation intercalation, it should also affect the efficiency of photocatalytic degradation of organic pollutants in the presence of dissolved inorganic salts. Moreover, taking advantage of the phenomenon of photointercalation during the decomposition of organic pollutants opens up completely new possibilities. For example, MoO_3 can act as a photocatalyst under anaerobic conditions, as with significantly enhanced efficiency as long as alkali metal ions are available in the solution. Thus process can be controlled using additional parameter usage of appropriate aqueous environment [66]. Here, the photoactivity of the bulk and exfoliated WO_3 towards decolorization of methylene blue were tested in the presence of 0.1 M Li_2SO_4, Na_2SO_4, K_2SO_4 or Cs_2SO_4. The progress in the photodegradation of MB under illumination is presented in Fig. 8 a, b. For comparison, photolysis tests were performed in the presence of alkali metal cations, but without a photocatalyst (Fig. S5a). In the case of bulk WO_3, the influence of the presence of alkali metal cations in the MB solution can be observed. After 2 h illumination, the photodegradation efficiency of MB in the presence of Li_2SO_4, Na_2SO_4, K_2SO_4 and Cs_2SO_4 reached 84 %, 63 %, 62 %, 54 %, respectively. The efficiency of MB degradation in solution

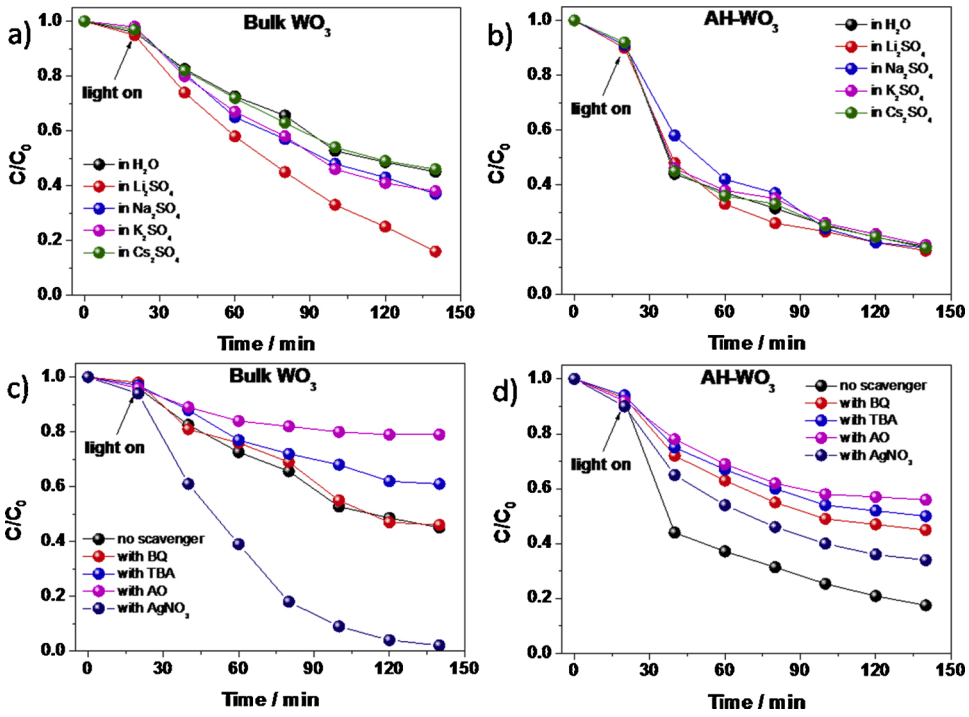

Fig. 8. Effect of different metal cations Li^+, Na^+, K^+, Cs^+ (a, b) and scavengers BQ, TBA, AO, $AgNO_3$ (c, d) on degradation efficiency of MB.

without the addition of inorganic salt is presented for comparison and reached 55 %. There is no doubt that the ion radius of the alkali metal ion present in the solution affects the efficiency of the MB photodegradation. The illumination of bulk WO_3 suspension leads to the photoexcitation of electrons to the conduction band. They may be utilized for reduction reactions or may be stored in its layered crystalline structure *via* alkali cation intercalation.

In the case of a large Cs^+ ion, the photodegradation efficiency is comparable to the experiment without the addition of salt. In the case of smaller cations, the improvement is noticeable. The intercalation process requires electrons, thus the presence Li^+, Na^+ and K^+ allows WO_3 to act as electron scavengers, consuming in reversible way photoelectrons changing the valence state of tungsten metal centers. The scavenging process of the photoexcited electrons leads to inhibition of the e^-/h^+ recombination. As a result, photoexcited holes may be utilized for photooxidation of MB more efficiently.

As can be seen, a similar effect has not been observed for the AH-WO_3, Fig. 8b. There are no substantial differences observed in photocatalytic degradation of MB due to electrolyte $LiSO_4$, Na_2SO_4, Cs_2SO_4 presence. The observations suggest that in the case of the lack of regular layer structure, alkali metal ions are not able to be inserted between the van der Waals gaps (because they do not exist). These results confirm the formation of 2-D exfoliated material.

The results of photocatalytic degradation of MB for bulk and exfoliated WO_3 in the presence of different scavengers are presented in Fig. 8 c and d. For a comparison, the photodegradation without scavengers has also been considered as a control process. In the case of the bulk WO_3, the results show that the addition of AO and TBA, which are used to be treated as the photoexcited holes (h^+) and hydroxyl radical ($^{\cdot}OH$) scavengers, significantly inhibits the photodegradation efficiency of MB. Thus, the degradation of MB is strictly related with direct photooxidation of dye adsorbed on the photocatalyst via holes from valence band. On the other hand, after the addition of BQ which is commonly used as a superoxide radicals scavenger, the MB photodecomposition efficiency is in similar level as in the case of the experiment without the addition of scavenger. It can be concluded that superoxide radicals do not participate in the photodegradation of organic dye. Thus, the main individuals responsible for dye photodegradation are holes and hydroxyl radicals. It was also confirmed by experiment performed in a presence of $AgNO_3$, which acts as electron scavenger. The MB degradation efficiency was significantly improved, because photoexcited electrons were consumed for Ag^+ reduction (or intercalation), what inhibits e^-/h^+ recombination [67]. However, the case with silver nitrate is not so straightforward because one may consider the modification of the catalyst with photoactive silver during the process. The same experimental procedure was performed for exfoliated WO_3. As it is shown in Fig. 8d, each scavenger negatively affected the MB photodegradation efficiency. Thus, it may be concluded that the way of methylene blue photodecomposition using AH-WO_3 is more complex and holes, hydroxyl radicals, superoxide radicals as well as photoelectrons participate in the process. For comparison, photolysis tests were performed in the presence of different scavengers, but without a photocatalyst (Fig. S5b).

The experimental results are summarized in diagram in Fig. 9.

Photoelectrochemical properties of the prepared electrodes were examined using the chronoamperometry (CA) and linear voltammetry (LV) technique recorded under intermittent illumination in different electrolytes (lithium, sodium, potassium and cesium sulfates) (Figs. 10 and 11). First, LV curves were measured. Then, electrodes were illuminated and polarized at 0.5 V (vs Ag/AgCl/3 M KCl) for 1 h (working conditions of the photoanode). In the next step, the LV and CA tests were repeated in order to compare the results with initial photocurrent. In the case of the bulk WO_3 electrodes, the type of electrolyte did not affect significantly the results and all the electrodes during the initial tests generated comparable but moderate photocurrent. In the case of potentiodynamic measurements (LV), the WO_3 photoanode generated photocurrent at potentials higher (more anodic) than the flatband

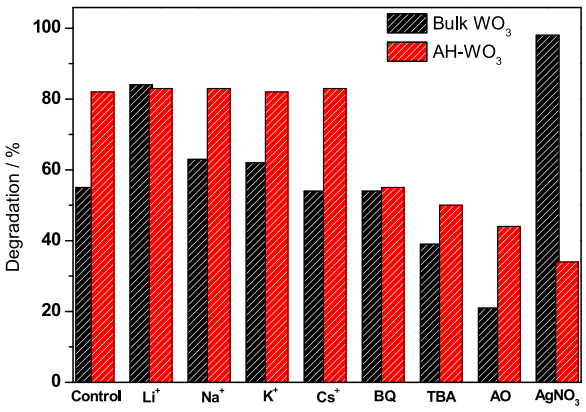

Fig. 9. Diagram presenting a summary of photocatalytic performance, measured degradation degree of MB.

potential, which is characteristic of n-type semiconductors. After one hour of operation in conditions of simultaneous illumination and polarization, repeated LV and CA tests shown that photoelectrochemical performance of electrodes decreased. However in the case of electrolyte containing Li^+ and K^+, the decrease in photocurrent was most pronounced. The negative effect of the presence of Li^+ dopant has been previously reported [22]. The LV curves were measured from -0.5 V (it was not a rest potential). As it is shown in Fig. 10, after pretreatment, the clear anodic humps on LV curves were registered for Li^+ Na^+ and K^+ electrolytes. We claim that anodic current is related to the deintercalation of alkali metal cations from the WO_3 layered structure. It was not expected, since the electrodes during the previous experiment were polarized anodically. However, it seems that during 1 h of measurement two different phenomenon occurs, photoinduced cation intercalation and deintercalation caused by anodic polarization. The anodic current recorded after an hour's measurement and the color change of the WO_3 film suggest that the equilibrium under given conditions is shifted towards the formation of intercalated material. Cesium ions intercalation requires the most significant distortion of WO_3 lattice [68]. Thus, in the case of the biggest Cs^+ ions, the effect was not so pronounced, which may indicate steric hindrance and mismatch of the ion radius to the size of van der Waals gaps in bulk WO_3. However, it is not the first time when WO_3 films were investigated as photoanodes in various aqueous electrolytes, including lithium, sodium and potassium sulphates [69]. Previously, the authors observed gradual decrease of photocurrent and significant differences in Faradaic efficiency of OER. It was claimed, that the hindering of photocurrent and O_2 evolution was observed due to the adsorbing of alkali metal cations on the active sites for oxygen evolving.

In general, the main conclusion of this experiment is that in the case of photoanodes based on metal oxides showing a layered structure, the type of cation in the electrolyte plays an important role and directly affects the recorded photocurrent of water oxidation. In the case of electrodes made of AH-WO_3, the effect of the cation type on the change of photoelectrochemical performance of photoanode was not expected due to the lack of regular, layered structure, unless we do not take into account photointercalation, but only blocking of active centers as reported here [69]. Noteworthy, the difference of recorded photocurrent before and after 1 h of operation in the case of Li^+, K^+ and Cs^+ were definitely smaller than the case of bulk material as it is shown in Fig. 11 (data are also presented separately in each row for used electrolyte Li_2SO_4, K_2SO_4, Na_2SO_4, Cs_2SO_4). These results support the concept of photointercalation. The proposed method of WO_3 modification improves its stability. Moreover, the characteristic anodic hump on LV curves was not recorded after 1 h of simultaneous polarization ($E = 0.5$ V) and illumination of AH-WO_3, in contrast to bulk WO_3. It suggests that in the case of unmodified, bulk WO_3, we are dealing with photointercalation and that phenomenon cannot occur in the case of

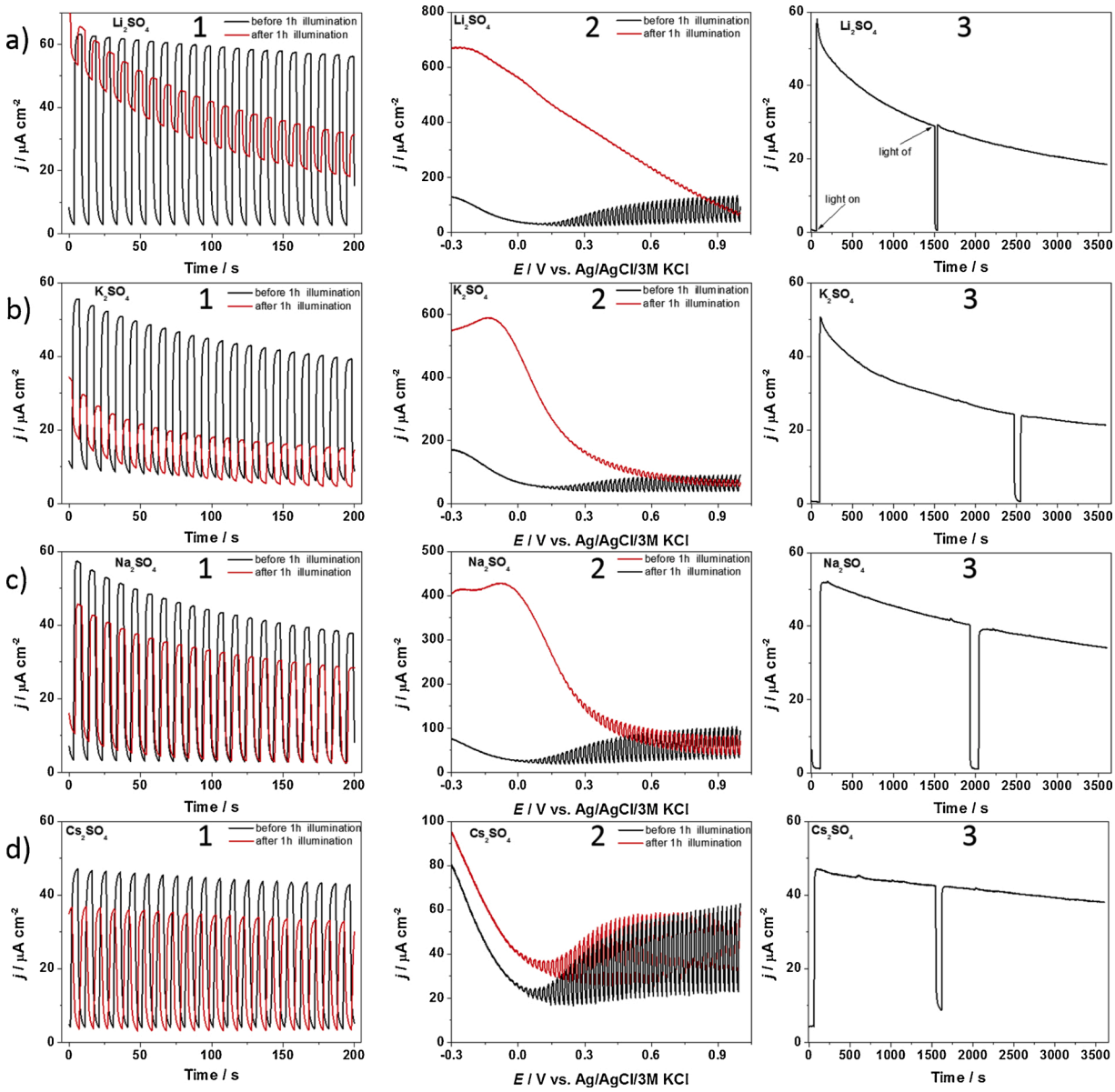

Fig. 10. The comparison of CA, LV curves of bulk WO_3 after and before illumination and the long-term chronoamperometry test (E = 0.5 V vs. Ag/AgCl (3 M KCl)) recorded during illumination of electrode. Measurements performed in various electrolytes a) Li_2SO_4, b) K_2SO_4, c) Na_2SO_4 and d) Cs_2SO_4.

exfoliated electrode material. However, as it is shown on the long-term CA test, the photocurrent increase in time for Na^+ containing electrolyte. Significant improvement of photoelectrochemical performance was achieved after 1 h of operation. The positive effect of the Na^+ presence on the photoactivity of monoclinic WO_3 was shown previously [70]. As it can be concluded, Na^+ ions positively affects also the photoelectrochemical performance of amorphous tungsten oxide, however the mechanism of the improvement is not clear.

The photocurrent densities registered at +0.5 V (chronoamperometry after 100 s) are listed in Table 1 with the difference between the current registered for a sample in the dark and under its illumination (Δj). The table shows a list of photocurrent recorded before and after 60 min of photoanode operation in various electrolytes.

Additionally, the Mott-Schottky analysis was performed for both types of electrodes. The influence of long-term illumination and anodic polarization has been investigated and the results are presented in the Fig. 12. In the case of exfoliated WO_3, the 30 min of simultaneous polarization and illumination does not affect the flat band potential as well as slope of Mott-Schottky plot. On the other hand, the significant changes were observed for bulk WO_3 electrode. The flat band potential stays more less the same and the value is similar to the one reported previously [71]. However the slope of the Mott-Schottky plot was twelve times lower for the electrode just after photoelectrochemical treatment. The slope of Mott-Schottky plot is inversely proportional to the donor concertation (N_d). In the case of the n-type semiconductors, N_d means electron donor concertation [72]. The significantly increased N_d value has been already reported for electrochemically reduced WO_3, which is in agreement with present observation [73], doped WO_3 [74,75] and hydrogen reduced WO_3 [76].

Here, excess of the electrons origins from the photoelectrochemical reaction. Generally, under anodic polarization photoexcited electrons should pass through the external circuit to the counterelectrode, but in the case of layered metal oxide material, some charges are stored in the electrode material via photoinduced intercalation.

In order to proof that presented in Figs. 10 and 11 changes of the photoelectrochemical performance are related to the photointercalation effect, EDX measurements of the electrode materials after polarization at 0.5 V vs Ag/AgCl (3 M KCl) in 0.1 M K_2SO_4 were performed. The EDX

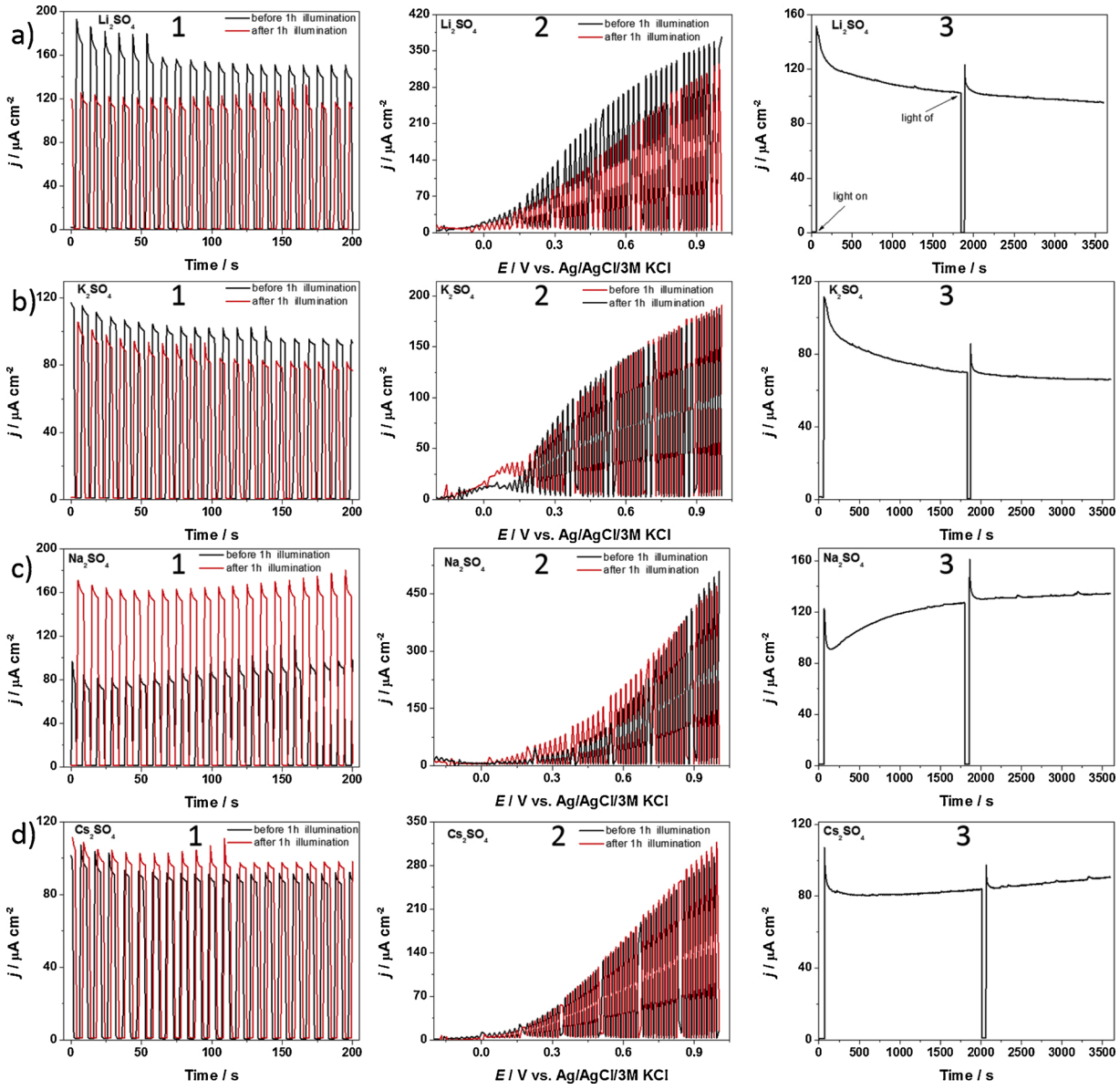

Fig. 11. The comparison of CA, LV curves of exfoliated WO_3 before and after illumination and the long-term chronoamperometry test (E = 0.5 V vs. Ag/AgCl (3 M KCl)) recorded during illumination of electrode. Measurements performed in various electrolytes a) Li_2SO_4, b) K_2SO_4, c) Na_2SO_4 and d) Cs_2SO_4.

Table 1
Photoelectrochemical activity (Δj) in various electrolytes at +0.5 V, measured before and after 1 h illumination.

Electrode	Li_2SO_4		K_2SO_4		Na_2SO_4		Cs_2SO_4	
	Δj, μA cm^{-2}							
	Before	after	before	after	before	after	before	after
Bulk WO_3	57	13.5	37.5	11.6	41.6	31.4	41.1	31.7
AH-WO_{3-x}	148	114	97.5	83.7	83.2	155	87.9	95.8

spectra of bulk WO_3 and AH-WO_3 after polarization at dark are presented in Fig. 13 a and d. Spectra consist peaks characteristic for W and O. In the case of bulk material, some residues of carbon were also detected (binder residue). No potassium was detected, that confirms that intercalaction does not occur at 0.5 V vs Ag/AgCl (3 M KCl) at the dark. As it was expected, the illumination of the polarized electrodes does not affect the EDX spectra of AH-WO_3, see Fig. 13 e and f. However, in the case of bulk material, EDX spectra (Fig. 13 b and c) consist a new peak at 3.31 keV that originate from intercalated potassium ions. Moreover, longer illumination leads to the increase of K content. Thus, it is direct evidence that intercalation phenomenon occurs for the anodically polarized bulk WO_3, while electrode material is illuminated.

4. Summary

We investigated the influence of alkali metal cation intercalation on photoelectrochemical and photocatalytic properties of bulk and exfoliated WO_3. The influence of the cation crystallographic ion radius on the

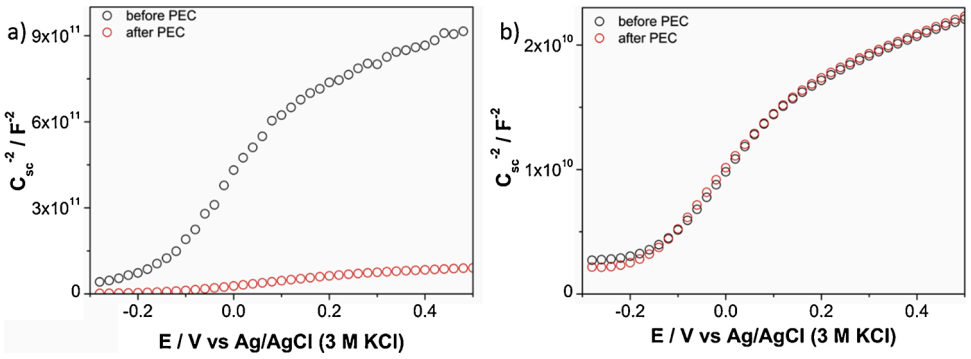

Fig. 12. The Mott–Schottky plot for a) bulk WO_3 and b) exfoliated WO_3 before and after illumination.

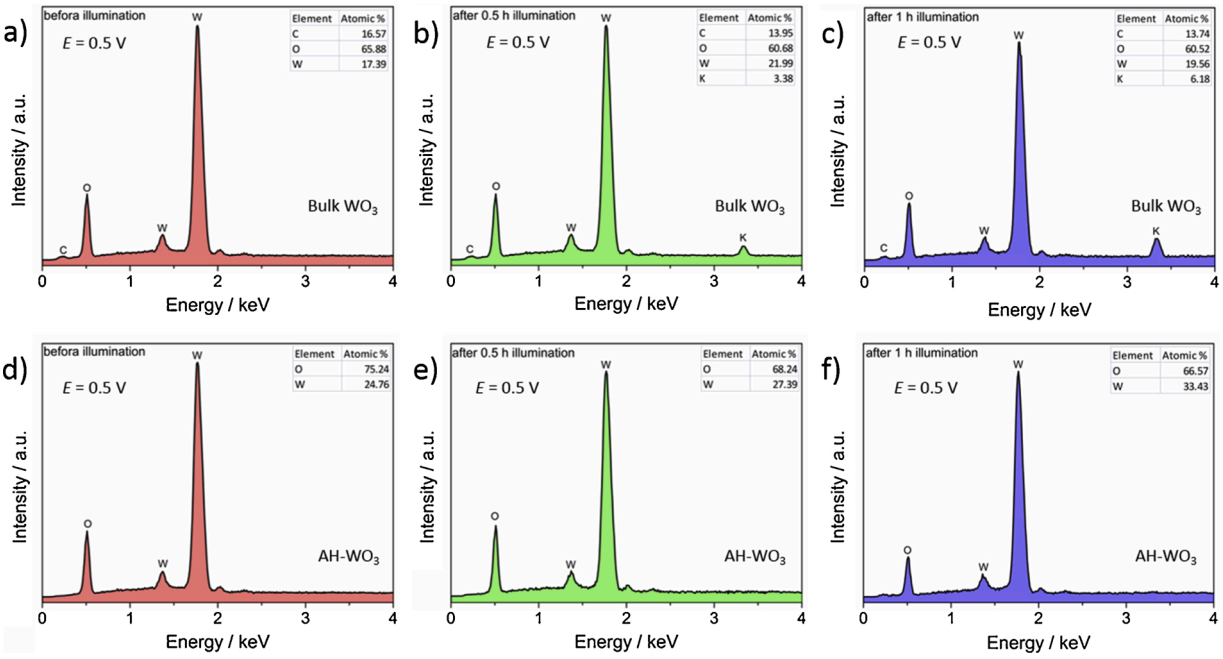

Fig. 13. EDX spectra of the (a-c) bulk WO_3 and (d-f) AH-WO_3 electrode materials after anodic polarization (0.5 V vs. Ag/AgCl (3 M KCl)) for 30 min at dark (a and d), 30 min under illumination (b and e), and 60 min under illumination (c and f).

tested properties was clearly observed only for bulk WO_3. We claim that the differences of WO_3 behaviour under simulated solar light illumination are related to the photointercalation phenomena. The process of photointercalation occurs only for non-exfoliated material in a form of powder as well as for electrode material even under anodic polarization. The main pathway of dye degradation is the direct reaction with photoexcited holes. The utilization of photoexcited electrons for photoinduced intercalation hindering adverse e^-/h^+ recombination and enhance efficiency of dye degradation. On the other hand, in the case of photoelectrochemical water splitting, the consumption of photoexcited electron negatively affect the measured photocurrent. In the case of the exfoliated WO_3, lack of regular, layered structure makes that photointercalation does not occur, thus the presence of cation in the electrolyte does not significantly affect the measured photoactivity. The presence of alkali metal cation in bulk WO_3 after long-term photointercalation has been confirmed using spectroscopic method. Summarizing, in the case of photocatalysts and photoanodes based on layered n-type semiconductors, the presence and the type of alkali metal cation in the electrolyte should be taken into account.

CRediT authorship contribution statement

M. Szkoda: Conceptualization, Methodology, Validation, Investigation, Resources, Writing - original draft, Writing - review & editing, Visualization, Supervision, Funding acquisition. **K. Trzciński:** Conceptualization, Investigation, Writing - original draft, Writing - review & editing, Visualization, Funding acquisition. **G. Trykowski:** Investigation. **M. Łapiński:** Investigation. **A. Lisowska-Oleksiak:** Validation, Supervision, Writing - review & editing.

Declaration of Competing Interest

The authors declare that they have no known competing financial interests or personal relationships that could have appeared to influence the work reported in this paper.

Acknowledgments

This work is financially supported by The National Centre for Research and Development via grant no LIDER/15/0088/L-10/18/NCBR/2019(*Integrated prototype of a photo-supercapacitor for energy storage obtained as a result of solar radiation conversion*).

Financial support of these studies from Gdańsk University of Technology by the DEC-3/2020/IDUB/I.3.3grant under the Argentum - 'Excellence Initiative - Research University' program is gratefully acknowledged.

Appendix A. Supplementary data

Supplementary material related to this article can be found, in the online version, at doi:https://doi.org/10.1016/j.apcatb.2021.120527.

References

[1] H. Tributsch, P.A. Briand, Photo-intercalation: possible application in solar energy devices, Appl. Phys. 23 (1980) 61–71.

[2] G. Betz, H. Tributsch, S. Fiechter, Photointercalation and optical information storage using $Cu_{6-x}PS_5I$, J. Electrochem. Soc. 131 (1984) 640.

[3] S.N. Lou, N. Yap, J. Scott, R. Amal, Y.H. Ng, Influence of MoO_3(110) crystalline plane on its self-charging photoelectrochemical properties, Sci. Rep. 4 (2014) 7428, https://doi.org/10.1038/srep07428.

[4] Z. Wang, H. Chiu, A. Paolella, K. Zaghib, Lithium photo-intercalation of CdS-sensitized WO_3 anode for energy storage and photoelectrochromic applications, ChemSusChem 12 (2019) 2220–2230, https://doi.org/10.1002/cssc.201803061.

[5] Y. Zhao, S. Balasubramanyam, R. Sinha, R. Lavrijsen, M.A. Verheijen, A.A. Bol, A. Bieberle-hu, Physical and chemical defects in WO_3 thin films and their impact on photoelectrochemical water splitting, ACS Appl. Energy Mater. 1 (2018) 11, https://doi.org/10.1021/acsaem.8b00849.

[6] W.J. Lee, P.S. Shinde, G.H. Go, E. Ramasamy, Ag grid induced photocurrent enhancement in WO_3 photoanodes and their scale-up performance toward photoelectrochemical H_2 generation, Int. J. Hydrogen Energy 36 (2011) 5262–5270, https://doi.org/10.1016/j.ijhydene.2011.02.013.

[7] H. Qi, J. Wolfe, D. Wang, H.J. Fan, D. Fichou, Z. Chen, Triple-layered nanostructured WO_3 photoanodes with enhanced photocurrent generation and superior stability for photoelectrochemical solar energy conversion, Nanoscale. 6 (2014) 13457–13462, https://doi.org/10.1039/c4nr03982c, doi:10.1039/c4nr03982c.

[8] S.J. Hong, H. Jun, P.H. Borse, J.S. Lee, Size effects of WO_3 nanocrystals for photooxidation of water in particulate suspension and photoelectrochemical film systems, Int. J. Hydrogen Energy 34 (2009) 3234–3242, https://doi.org/10.1016/j.ijhydene.2009.02.006.

[9] C. Bechinger, E. Wirth, P. Leiderer, Photochromic coloration of WO_3 with visible light, Appl. Phys. Lett. 68 (1996) 2834, https://doi.org/10.1063/1.116340.

[10] K. Mizushima, P.C. Jones, P.J. Wiseman, J.B. Goodenough, $LixCoO_2$ (0<x<-1): a new cathode material for batteries of high energy density, Mater. Res. Bull. 15 (1980) 783–789, https://doi.org/10.1016/0025-5408(80)90012-4.

[11] M.S. Whittingham, Electrical energy storage and intercalation chemistry, Science 192 (1976) 1126–1127, https://doi.org/10.1126/science.192.4244.1126.

[12] M.S. Whittingham, Chemistry of intercalation compounds: metal guests in chalcogenide hosts, Prog. Solid State Chem. 12 (1978) 41–99, https://doi.org/10.1016/0079-6786(78)90003-1.

[13] C.G. Granqvist, Electrochromic tungsten oxide films: review of progress 1993–1998, Sol. Energy Mater. Sol. Cells 60 (2000) 201–262, https://doi.org/10.1016/S0927-0248(99)00088-4, doi:.

[14] R. Wen, C.G. Granqvist, G.A. Niklasson, Eliminating degradation and uncovering ion-trapping dynamics in electrochromic WO_3 thin films, Nat. Mater. 14 (2015) 996–1001, https://doi.org/10.1038/NMAT4368.

[15] Y. Soo, Tuning of the crystal engineering and photoelectrochemical properties of crystalline tungsten oxide for optoelectronic device applications, CrystEngComm. 17 (2015) 6070–6093, https://doi.org/10.1039/c5ce00900f.

[16] M. Szkoda, K. Trzciński, K. Siuzdak, A. Lisowska-Oleksiak, Photocatalytical properties of maze-like MoO_3 microstructures prepared by anodization of Mo plate, Electrochim. Acta 228 (2017) 139–145, https://doi.org/10.1016/j.electacta.2017.01.064.

[17] M. Szkoda, K. Trzciński, M. Łapiński, A. Lisowska-Oleksiak, Photoinduced K^+ intercalation into MoO_3/FTO photoanode - the impact on the photoelectrochemical performance, Electrocatal. 11 (2020) 111–120.

[18] S.J. Calero, P. Ortiz, A.F. Onate, M.T. Cortes, Effect of proton intercalation on photo-activity of WO_3 anodes for water splitting, Int. J. Hydrog. Energy. 41 (2016) 4922–4930, https://doi.org/10.1016/j.ijhydene.2015.12.155.

[19] X. Yin, W. Qiu, W. Li, K. Wang, X. Yang, L. Du, Y. Liu, J. Li, Effects of alkali ion on boosting WO_3 photoelectrochemical performance by electrochemical doping, Int. J. Hydrogen Energy 45 (2020) 19257–19266, https://doi.org/10.1016/j.ijhydene.2020.05.057.

[20] S. Tosoni, C. Di Valentin, G. Pacchioni, Effect of alkali metals interstitial doping on structural and electronic properties of WO_3, J. Phys. Chem. C. 118 (2014) 3000–3006.

[21] Y. Cui, Q. Wang, G. Yang, Y. Gao, Journal of Solid State Chemistry Electronic properties, optical properties and diffusion behavior of WO_3 with H+, Li+ and Na+ intercalated ions : a first-principles study, J. Solid State Chem. 297 (2021), 122082, https://doi.org/10.1016/j.jssc.2021.122082.

[22] R. Solarska, B.D. Alexander, A. Braun, R. Jurczakowski, G. Fortunato, M. Stiefel, T. Graule, J. Augustynski, Tailoring the morphology of WO_3 films with substitutional cation doping: effect on the photoelectrochemical properties, Electrochim. Acta 55 (2010) 7780–7787, https://doi.org/10.1016/j.electacta.2009.12.016.

[23] Q. Mi, Y. Ping, Y. Li, B. Cao, B.S. Brunschwig, P.G. Khalifah, G.A. Galli, H.B. Gray, N.S. Lewis, Thermally stable N_2-Intercalated WO_3 photoanodes for water oxidation, J. Am. Chem. Soc. 134 (2012) 18318–18324, https://doi.org/10.1021/ja3067622.

[24] D. Li, R. Takeuchi, D. Chandra, K. Saito, T. Yui, M. Yagi, Visible light-driven water oxidation on an in situ N 2 -Intercalated WO_3 nanorod photoanode synthesized by a dual-functional structure-directing agent, ChemSusChem. 11 (2018) 1151–1156, https://doi.org/10.1002/cssc.201702439.

[25] S.S. Kalanur, H. Seo, Intercalation of barium into monoclinic tungsten oxide nanoplates for enhanced photoelectrochemical water splitting, Chem. Eng. J. 355 (2019) 784–796, https://doi.org/10.1016/j.cej.2018.08.210.

[26] D. Nagy, D. Nagy, I.M. Szilagyi, X. Fan, Effect of the morphology and phases of WO_3 nanocrystals on their photocatalytic efficiency, RSC Adv. 6 (2016) 33743–33754, https://doi.org/10.1039/c5ra26582g.

[27] M. Szkoda, Z. Zarach, K. Trzciński, G. Trykowski, A.P. Nowak, An easy and ecological method of obtaining hydrated and non-crystalline WO_{3-x} for application in supercapacitors, Materials 13 (2020) 1925, https://doi.org/10.3390/ma13081925.

[28] M. Szkoda, Z. Zarach, K. Trzciński, A.P. Nowak, An aqueous exfoliation of WO_3 as a route for counterions fabrication — improved photocatalytic and capacitive properties of Polyaniline/WO_3 composite, Materials 13 (2020) 5781.

[29] K. Trzciński, M. Szkoda, A. Herman, A. Borowska-Centkowska, A. Lisowska-Oleksiakm does the low optical band gap of yellow $Bi3YO_6$ guarantee the photocatalytical activity under visible light illumination? J. Solid State Electrochem. 22 (2018) 2095–2105.

[30] S. Chen, Y. Xiao, Y. Wang, Z. Hu, H. Zhao, W. Xie, A facile approach to prepare black TiO_2 with oxygen vacancy for enhancing photocatalytic activity, Nanomater. 8 (2018) 245, https://doi.org/10.3390/nano8040245.

[31] M. Szkoda, K. Trzciński, A.P. Nowak, M. Gazda, M. Sawczak, A. Lisowska-Oleksiak, The effect of morphology and crystalline structure of Mo/MoO_3 layers on photocatalytic degradation of water organic pollutants, Mater. Chem. Phys. 248 (2020), 122908, https://doi.org/10.1016/j.matchemphys.2020.122908.

[32] X. Zhang, X. Wang, X. Yi, L. Liu, J. Ye, D. Wang, Metal-reduced WO_{3-x} electrodes with tunable plasmonic resonance for enhanced photoelectrochemical water splitting, ACS Appl. Energy Mater. 3 (2020) 3569–3576, https://doi.org/10.1021/acsaem.0c00086.

[33] K. Manthiram, A.P. Alivisatos, Tunable localized surface plasmon resonances in tungsten oxide nanocrystals, J. Am. Chem. Soc. 134 (2012) 3995–3998, https://doi.org/10.1021/ja211363w.

[34] H. Tang, Z. Tang, J. Bright, B. Liu, X. Wang, G. Meng, N. Wu, Visible-light localized surface plasmon resonance of WO_{3-x} nanosheets and its photocatalysis driven by plasmonic hot carriers, ACS Sustain. Chem. Eng. 9 (2021) 1500–1506, https://doi.org/10.1021/acssuschemeng.0c08140.

[35] A.T.H. Cheng, M. Klapproth, A. Sagaltchik, S. Li, Ordered mesoporous $WO_{2.83}$: selective reductionsynthesis, exceptional localized surface plasmonresonance and enhanced hydrogen evolutionreaction activity, J. Mater. Chem. A. 6 (2018) 2249–2256, https://doi.org/10.1039/c7ta09579a.

[36] Z. Lou, M. Zhu, X. Yang, Y. Zhang, M.-H. Whangbo, B. Li, B. Huang, Continual injection of photoinduced electrons stabilizing surface plasmon resonance of non-elemental-metal plasmonic photocatalyst CdS/WO_{3-x} for efficient hydrogen generation, Appl. Catal. B Environ. 226 (2018) 10–15, https://doi.org/10.1016/j.apcatb.2017.12.023.

[37] V.G.A. Paliwal, A. Sharma, M. Tomar, Optical properties of WO_3 thin films using surface plasmon resonance technique, J. Appl. Phys. 115 (2014), 043104, https://doi.org/10.1063/1.4862962.

[38] D.E. Mustafa, T. Yang, Z. Xuan, S. Chen, H. Tu, A. Zhang, Surface plasmon coupling effect of gold nanoparticles with different shape and size on conventional surface plasmon resonance signal, Plasmonics. 5 (2010) 221–231, https://doi.org/10.1007/s11468-010-9141-z.

[39] H. Guo, F. Ruan, L. Lu, J. Hu, J. Pan, Z. Yang, B. Ren, Correlating the shape, surface plasmon resonance, and surface-enhanced Raman scattering of gold nanorods, J. Phys. Chem. C. 113 (2009) 10459–10464, https://doi.org/10.1021/jp9019427.

[40] J. Zhang, P. Zhang, T. Wang, J. Gong, Monoclinic WO_3 nanomultilayers with preferentially exposed (002) facets for photoelectrochemical water splitting, Nano Energy 11 (2015) 189–195, https://doi.org/10.1016/j.nanoen.2014.10.021.

[41] K.J. Patel, C.J. Panchal, V.A. Kheraj, M.S. Desai, Growth, structural, electrical and optical properties of the thermally evaporated tungsten trioxide (WO_3) thin films, Mater. Chem. Phys. 114 (2009) 475–478, https://doi.org/10.1016/j.matchemphys.2008.09.071.

[42] P.A. Shinde, A.C. Lokhande, N.R. Chodankar, A.M. Patil, J.H. Kim, C.D. Lokhande, Temperature dependent surface morphological modifications of hexagonal WO_3 thin films for high performance supercapacitor application, Electrochim. Acta 224 (2017) 397–404, https://doi.org/10.1016/j.electacta.2016.12.066.

[43] R.S. Datta, F. Haque, M. Mohiuddin, B.J. Carey, N. Syed, A. Zavabeti, B. Zhang, H. Khan, K.J. Berean, J.Z. Ou, N. Mahmood, T. Daeneke, K. Kalantar-zadeh, Highly active two dimensional α-MoO_{3-x} for the electrocatalytic hydrogen evolution reaction, J. Mater. Chem. A. 5 (2017) 24223–24231, https://doi.org/10.1039/c7ta07705j.

[44] J. Torres, J.E. Alfonso, Optical characterization of MoO_3 thin films produced by continuous wave CO_2 laser-assisted evaporation, Thin Solid Films 478 (2005) 146–151, https://doi.org/10.1016/j.tsf.2004.10.027.

[45] M. Nistor, A. Rougier, Low temperature Si doped ZnO thin films for transparent conducting oxides, Sol. Energy Mater. Sol. Cells 95 (2011) 2357–2362, https://doi.org/10.1016/j.solmat.2011.04.006.

[46] R. Azimirad, N. Naseri, O. Akhavan, A.Z. Moshfegh, Hydrophilicity variation of WO_3 thin films with annealing temperature, J. Phys. D Appl. Phys. 40 (2007) 1134, https://doi.org/10.1088/0022-3727/40/4/034.
[47] A.P. Shpak, A.M. Korduban, M.M. Medvedskij, V.O. Kandyba, XPS studies of active elements surface of gas sensors based on WO_{3-x} nanoparticles, J. Electron Spectros. Relat. Phenomena 158 (2007) 172–175, https://doi.org/10.1016/j.elspec.2006.12.059.
[48] S. Poongodi, P.S. Kumar, Y. Masuda, D. Mangalaraj, N. Ponpandian, C. Viswanathan, S. Ramakrishna, Synthesis of hierarchical WO_3 nanostructured thin fi lms with enhanced electrochromic performance for switchable smart windows, RSC Adv. 5 (2015) 96416–96427, https://doi.org/10.1039/c5ra19177g.
[49] K. Kalantar-zadeh, A. Vijayaraghavan, M. Ham, H. Zheng, M. Breedon, M.S. Strano, Synthesis of atomically thin WO_3 sheets from hydrated tungsten trioxide, Chem. Mater. 22 (2010) 5660–5666, https://doi.org/10.1021/cm1019603.
[50] M. Boulova, A. Gaskov, G. Lucazeau, Tungsten oxide reactivity versus CH_4, CO and NO_2 molecules studied by Raman spectroscopy, Sens. Actuators B Chem. 81 (2001) 99–106.
[51] M. Pham Thi, G. Velasco, Raman study of WO3 thin films, Solid State Ionic. 14 (2000) 217–220.
[52] S. Lee, H.M. Cheong, C.E. Tracy, A. Mascarenhas, A.W. Czanderna, K. Satyen, A. W. Czanderna, S.K. Deb, Electrochromic coloration efficiency of a-WO_{3-y} thin films as a function of oxygen deficiency of oxygen deficiency, Appl. Phys. Lett. 75 (1999) 1541, https://doi.org/10.1063/1.124782.
[53] E. Cazzanelli, C. Vinegoni, G. Mariotto, A. Kuzmin, J. Purans, Low-temperature polymorphism in tungsten trioxide powders and its dependence on mechanical treatments, J. Solid State Chem. 143 (1999) 24–32.
[54] N. Minh Vuong, D. Kim, H. Kim, Porous Au-embedded WO_3nanowire structure for efficient detection of CH_4 and H_2S, Sci. Rep. 5 (2015) 1–13, https://doi.org/10.1038/srep11040.
[55] K.V.A. Kumar, L. Chandana, P. Ghosal, C. Subrahmanyam, Simultaneous photocatalytic degradation of p-cresol and Cr (VI) by metal oxides supported reduced graphene oxide, Mol. Catal. 451 (2018) 87–95, https://doi.org/10.1016/j.mcat.2017.11.014.
[56] S. Songara, V. Gupta, M. Kumar Patra, J. Singh, L. Saini, G. Siddaramana Gowd, S. Raj Vadera, N. Kumar, Tuning of crystal phase structure in hydrated WO_3 nanoparticles under wet chemical conditions and studies on their photochromic properties, J. Phys. Chem. Solids 73 (2012) 851–857, https://doi.org/10.1016/j.jpcs.2012.02.020.
[57] L. Gao, X. Wang, Z. Xie, W. Song, L. Wang, X. Wu, F. Qu, D. Chen, G. Shen, High-performance energy-storage devices based on WO_3 nanowire arrays/carbon cloth integrated electrodes, J. Mater. Chem. A. 1 (2013) 7167–7173, https://doi.org/10.1039/c3ta10831g.
[58] S.R. Bathe, P.S.Ã. Patil, Electrochromic characteristics of fibrous reticulated WO_3 thin films prepared by pulsed spray pyrolysis technique, Sol. Energy Mater. Sol. Cells 91 (2007) 1097–1101, https://doi.org/10.1016/j.solmat.2007.03.005.
[59] W. Cheng, E. Baudrin, J.I. Zink, Synthesis and electrochromic properties of mesoporous tungsten oxide, J. Mater. Chem. 11 (2001) 92–97, https://doi.org/10.1039/b003192p.
[60] J. Wang, C. Liu, Preparation of 2D WO_3 nanomaterials with enhanced catalytic activities: current status and perspective, ChemBioEng. 2 (2015) 335–350, https://doi.org/10.1002/cben.201500014.
[61] M.R. Allen, A. Thibert, E.M. Sabio, N.D. Browning, D.S. Larsen, F.E. Osterloh, Evolution of physical and photocatalytic properties in the layered titanates $A_2Ti_4O_9$ (A = K, H) and in nanosheets derived by chemical, Chem. Mater. 22 (2010) 1220–1228, https://doi.org/10.1021/cm902695r.
[62] Y. Ma, Y. Jia, L. Wang, M. Yang, Y. Bi, Y. Qi, Exfoliated thin Bi_2MoO_6 nanosheets supported on WO_3 electrode for enhanced photoelectrochemical water splitting, Appl. Surf. Sci. 390 (2016) 399–405, https://doi.org/10.1016/j.apsusc.2016.08.116.
[63] G. Guan, J. Xia, S. Liu, Y. Cheng, S. Bai, S.Y. Tee, Electrostatic-driven exfoliation and hybridization of 2D nanomaterials, Adv. Mater. 29 (2017), 1700326, https://doi.org/10.1002/adma.201700326.
[64] A.I. Gavrilyuk, Photochromism in WO_3 thin fims, Electrochim. Acta 44 (1999) 3027–3037, https://doi.org/10.1016/S0013-4686(99)00017-1.
[65] O. Avellaneda, L.O.S. Bulho, Photochromic properties of WO_3 and WO_3:x (X = Ti, Nb, Ta and Zr) thin films, Solid State Ion. 165 (2003) 117–121, https://doi.org/10.1016/j.ssi.2003.08.023.
[66] M. Szkoda, K. Trzci, M. Klein, K. Siuzdak, The influence of photointercalaction and photochromism effects on the photocatalytic properties of electrochemically obtained maze-like MoO3 microstructures, Sep. Purif. Technol. 197 (2018) 382–387, https://doi.org/10.1016/j.seppur.2018.01.033.
[67] S. Wang, D. Chen, F. Niu, N. Zhang, L. Qin, Y. Huang, Pd cocatalyst on Sm-doped $BiFeO_3$ nanoparticles: synergetic effect of a Pd cocatalyst and samarium doping on photocatalysis, RSC Adv. 6 (2016) 34574–34587, https://doi.org/10.1039/c6ra01140c.
[68] S. Tosoni, C. Di Valentin, G. Pacchioni, Effect of alkali metals interstitial doping on structural and electronic properties of WO_3, J. Phys. Chem. C. 118 (2014) 3000–3006, https://doi.org/10.1021/jp4123387.
[69] J.C. Hill, K.S. Choi, Effect of electrolytes on the selectivity and stability of n-type WO_3 photoelectrodes for use in solar water oxidation, J. Phys. Chem. C. 116 (2012) 7612–7620, https://doi.org/10.1021/jp209909b.
[70] M. Sarnowska, K. Bienkowski, P.J. Barczuk, R. Solarska, J. Augustynski, Highly efficient and stable solar water splitting at (Na)WO_3 photoanodes in acidic electrolyte assisted by non-noble metal oxygen evolution catalyst, Adv. Energy Mater. 6 (2016), 1600526, https://doi.org/10.1002/aenm.201600526.
[71] J.S.L.S.J. Hong, S. Lee, J.S. Jang, Heterojunction $BiVO_4$/WO_3 electrodes for enhanced photoactivity of water oxidation, Energy Environ. Sci. 4 (2011) 1781–1787, https://doi.org/10.1039/c0ee00743a.
[72] A.W. Btt, Electrochemistry of semiconductors, Curr. Sep. 3 (1998) 87–91.
[73] J. Zhao, E. Olide, F.E. Osterloh, Enhancing majority carrier transport in WO_3Water oxidation photoanode via electrochemical doping, J. Electrochem. Soc. 162 (2014) H65–H71, https://doi.org/10.1149/2.0871501jes.
[74] T. Zhang, Z. Zhu, H. Chen, Y. Bai, S. Xiao, X. Zheng, Q. Xue, S. Yang, Iron-doping-enhanced photoelectrochemical water splitting performance of nanostructured WO_3: a combined experimental and theoretical study, Nanoscale. 7 (2015) 2933–2940, https://doi.org/10.1039/C4NR07024K.
[75] S.S. Kalanur, I.-H. Yoo, K. Eom, H. Seo, Enhancement of photoelectrochemical water splitting response of WO_3 by means of Bi doping, J. Catal. 357 (2018) 127–137, https://doi.org/10.1016/j.jcat.2017.11.012.
[76] Y.L.G. Wang, Y. Ling, H. Wang, X. Yang, C. Wang, J.Z. Zhang, Hydrogen-treated WO_3 nanoflakes show enhanced photostability, Energy Environ. Sci. 5 (2012) 6180–6187, https://doi.org/10.1039/c2ee03158b.